Meandering jets in shallow rectangular reservoirs: POD analysis and identification of coherent structures

Y. Peltier [1], S. Erpicum, P. Archambeau, M. Pirotton & B. Dewals

University of Liege (ULg), ArGEnCo Department, Research Group HECE. Chemin des Chevreuils 1, Bat B52/3 +1, 4000, Liège, Belgium.

Abstract:

The effect of the shallowness on meandering jets in a shallow rectangular reservoir is investigated. Four meandering flows were investigated in an experimental shallow rectangular reservoir. Their boundary conditions were chosen to cover a large range of friction numbers (defined with the sudden expansion width). Due to the unsteady characteristics of the flows, a Proper Orthogonal Decomposition of the fluctuating part of the surface velocity fields measured using LSPIV was used for discriminating the flow structures responsible for the meandering of the jet. Less than 1 % of the calculated POD modes significantly contribute to the meandering of the jet and two types of instability are in competition in such a flow configuration. The sinuous mode is the dominant mode in the flow and it induces the meandering of the flow, while the varicose mode is a source of local mixing and weakly participates to the flow. The fluctuating velocity fields were then reconstructed using the POD modes corresponding to 80% of the total mean fluctuating kinetic energy and the coherent structures were identified using the residual vorticity, their centres being localised using a topology algorithm. The trajectories of the structures centres emphasize that at high friction number the coherent structures are small and laterally paired in the near, middle and far fields of the jet, while with decreasing friction number the structures merge into large horizontal vortices in the far-field of the jet, their trajectories showing more variability in space and time. The analysis of the stability regime finally reveals that the sinuous mode is convectively unstable and may become absolutely unstable at the end of the reservoir when the friction number is small.

Keywords:

Shallow rectangular reservoir, meandering jet, Proper Orthogonal Decomposition, coherent structures, flow topology

[1] Corresponding author: Y.Peltier@ulg.ac.be

1. INTRODUCTION

Shallow rectangular reservoirs are commonly used for water-management in human constructions and in natural environments. Two types of reservoirs are generally distinguished:

(1) The storage reservoirs, which are used for flood-control or hydro-power generation, and are designed to contain a great volume of clear water.

(2) The settling reservoirs, which are used for storm-water treatment and protection of irrigation systems, and are designed to trap pollutants and/or sediments.

As shown by Dufresne *et al.* (2012), most design methods only take into account the volume of the reservoir, without considering its shape nor the detailed characteristics of the flow patterns. However, an optimal sizing and management of these reservoirs, in terms of sediment transport and/or water storage, can only be reached based on a detailed knowledge of the flow fields developing in the reservoir (Dufresne *et al.* 2012; Dufresne *et al.* 2010b; Peltier *et al.* 2013). Flows in shallow rectangular reservoirs are indeed complex, involving large-scale horizontal coherent structures responsible for momentum transfers, which strongly affect sediment transport by the flow (Aloui and Souhar 2000; Camnasio *et al.* 2011; Canbazoglu and Bozkir 2004; Dewals *et al.* 2008; Dufresne *et al.* 2010a; Kantoush *et al.* 2008; Mullin *et al.* 2003; Oca and Masaló 2007; Peltier *et al.* 2014). For instance Dufresne *et al.* (2012) showed for different shallow rectangular reservoirs that the sediment trapping efficiency depends on the number of reattachment points present in the flow field (*i.e.* presence or not of large recirculation zones). This is an important aspect to be taken into account in the design of such reservoirs; otherwise, it may lead to high unexpected maintenance costs (additional operations of sediment removal).

The complete description of the different types of flows occurring in shallow reservoirs, even in the simplest geometric configuration (rectangular), is still an ongoing challenge as some regimes are still not well understood. The regime of the flow developing in shallow rectangular reservoirs and therefore the type of the flow patterns, depends on the Froude number at the reservoir inlet, F, and on the reservoir geometry, characterized by the shape factor defined as $\mathsf{SF} = L/\Delta B^{0.6} b^{0.4}$ by Dufresne *et al.* (2010a) (L the reservoir length, b the width of the inlet channel and ΔB the width of the sudden expansion). Peltier *et al.* (2014) showed that the flow can be:

- Symmetric (F < 0.21 and SF < 6.2): the jet is straight from the inlet to the outlet of the reservoir and symmetric recirculation zones develop on both sides of the jet
- Asymmetric (SF > 8.1): the jet impacts one or several times the lateral wall despite the axisymmetric geometry of the reservoir and different sizes of recirculation zones develop in the flow
- Meandering (F > 0.21 and SF < 6.2): the jet periodically and spatially oscillates from the inlet to the outlet of the reservoir, these oscillations slightly deforming the recirculation zones outside of the jet
- Unstable: when F is close to 0.21 and SF < 6.2 or when F > 0.21 and 6.2 < SF < 8.1, the regime of the jet randomly changes; in the same experiment, the jet can either go straight (with or without meandering patterns) from the inlet to the outlet or impact one or several times the lateral wall before going out.

Symmetric, asymmetric and unstable flows in shallow rectangular reservoirs are now well documented in literature, which enabled the development of accurate numerical models able to reproduce those flow features (Camnasio *et al.* 2013; Dewals *et al.* 2008; Dufresne *et al.* 2011; Khan *et al.* 2013; Peng *et al.* 2011; Stovin and Saul 2000). In contrast, very few studies deal with meandering jet in shallow rectangular reservoirs. Aspect ratios, geometries and hydraulic conditions encountered in literature generally differ from those leading to meandering jet in shallow rectangular reservoir (flows in cylinders with an expanded part (Guo *et al.* 1998), submerged nozzle injecting water into a vertical rectangular cavity (Honeyands and Molloy 1995; Lawson and Davidson 2001), vertical plume of effluent material (Landel *et al.* 2012)). The closest configurations to shallow rectangular reservoirs are those investigating plane turbulent jets entering a bounded fluid layer (Canestrelli *et al.* 2014; Chen and Jirka 1998; Dracos *et al.* 1992; Giger *et al.* 1991; Rowland *et al.* 2009). These configurations are encountered in water cooling of equipment or represent a river entering a water body at rest (*e.g.* a river mouth). They provide some fundamental insights into the physics of meandering flows in shallow rectangular reservoirs. Dracos *et al.* (1992) thus showed that the water depth, H, is the appropriate length-scale to consider for the normalisation of the results instead of the width of the inlet channel, b and they found that the instabilities of the jet are affected by the lateral wall when $B/2/l < 10$ ($B/2$ the half-width of the flow domain and l the characteristic length of the jet represented by the half-width of the jet $b_{1/2} = 0.881\times l$). Through a linear stability analysis of an idealized jet, Chen and Jirka (1998) and Socolofsky and Jirka (2004) brought a first explanation to the mechanism of the jet meandering. The presence of two inflection points in the velocity profile of the jet flow is the source of two instability modes (sinuous and varicose). These modes are usually convectively unstable, the sinuous one being the most unstable. The relative weight of these two modes governs the occurrence of meandering jets. Moreover Chen and Jirka (1998) observed that "*the role of viscosity is quite small and the stability of the jet is mainly controlled by bed friction*". Finally, by modelling a river mouth, Rowland *et al.* (2009) highlighted that the meandering of the jet significantly affects turbulent intensities, lateral shear stress distributions and momentum transfers, which induce changes in the local mixing and dispersal of scalars. Consistent with these previous findings, Peltier *et al.* (2013) showed with numerical simulations including sediment transport and morphodynamics, that the additional momentum transfer of the meandering jet induces a larger spreading of the sediments on both sides of the jet compared to configurations without a meandering jet: the trapping efficiency of the reservoir increases by a factor 1.7. However, many unanswered questions remain as far as flows in real-world shallow rectangular reservoirs are concerned and additional studies are needed. Knowledge gaps include among others, the effect of the instability modes on the characteristics of the meandering jet, as well as the influence of the shallowness on the flow patterns. Furthermore, additional data will be needed for better understanding how the meandering of the jet affects the transport of sediment particles and pollutants, and as a result, improve the design hydraulic works made for trapping polluted sediments.

In this paper, we analyse the physics of four meandering jets having very different inflow conditions in terms of Friction number. The main purpose of the study is to understand how the shallowness of the reservoir affects the coherent structures within the meandering jet. Experiments were carried out with clear water and the flow velocity was measured by Large Scale Particle Image Velocity (LSPIV) (Hauet *et al.* 2008a). The fluctuating velocity fields are first analysed using a Proper Orthogonal Decomposition (POD). After the identification of the POD modes corresponding to the coherent structures, the fluctuating velocity fields are reconstructed based on these modes. The coherent structures are identified using a criterion based on the residual vorticity (Kolář 2007), while the centres of the structures are identified using a topology algorithm (Depardon *et al.* 2006). The results are correlated with the flow shallowness and the stability of the flows is finally discussed.

2. PROPER ORTHOGONAL DECOMPOSITION (POD)

Meandering jets are characterised by periodical oscillations as depicted in Fig. 1, which are a combination of several sizes of energetic structures mainly controlled by the particular geometry of the reservoir (Peltier *et al.* 2014). In this study, the discrimination of the structures within the flow with respect to their respective energy was performed using a modal decomposition of the fluctuating velocity fields: the Proper Orthogonal Decomposition (POD) (Berkooz *et al.* 1993; Holmes *et al.* 2012).

The POD can be carried out using two methods: (1) the direct method (Berkooz *et al.* 1993; Holmes *et al.* 2012) or (2) the snapshot method (Sirovich 1987). Both methods give similar results (Graftieaux *et al.* 2001). The snapshot method is faster when the number of spatial information in the measurement fields is greater than the number of measurement fields itself (*i.e.* so-called snapshots), and vice versa for the direct method. The size of the LSPIV computation grid in this study (9405 points) being similar to the number of snapshots (9000), both method would applied. Since the snapshot method was used in previous studies (Peltier *et al.* 2013; 2014), we decide to also employ this method for the present study. In the following paragraphs, a short description of the snapshot method used in this study is presented. It was coded in Matlab©.

Let $\boldsymbol{u}(\boldsymbol{x},t_i)$ be a collection of N ($N \in \mathbb{N}^*$) instantaneous horizontal velocity fields, measured at a regular time interval, Δt, in the discrete physical space $\Omega \subset \mathbb{R}^2$. These velocity fields are square integrable functions ($\boldsymbol{u}(\boldsymbol{x},t_i) \in L^2(\Omega)$) and they are split into a steady part, $\langle \boldsymbol{u}(\boldsymbol{x},t) \rangle_N$, and a fluctuating part, $\boldsymbol{u}'(\boldsymbol{x},t)$, with $\langle \ \rangle_N$ denoting the average over the N snapshots.

The snapshot method provides an orthogonal basis of M temporal coefficients, $a_m(t_i)$ ($m \in \{1, \ldots, M \leq N\}$ M and $N \in \mathbb{N}^*$), which combined to an orthonormal basis of M spatial function

$\boldsymbol{\phi}_m(\boldsymbol{x})$ of $L^2(\Omega)$, called spatial modes, best fits $\boldsymbol{u'}(\boldsymbol{x},t)$ in the least-square sense (Brevis and García-Villalba 2011):

$$\min\left(\frac{1}{N}\sum_{i=1}^{N}\left\|\boldsymbol{u'}(\boldsymbol{x},t_i)-\sum_{m=1}^{M\leq N}a_m(t_i)\boldsymbol{\phi}_m(\boldsymbol{x})\right\|_{L^2}^2\right) \tag{1}$$

with $\| \ \|_{L^2} = \sqrt{(\ , \ )_{L^2}}$ the induced norm in $L^2(\Omega)$ and $(\ , \ )_{L^2}$ the inner product for $L^2(\Omega)$. According to Couplet *et al.* (2003), "the POD basis is optimal by construction, *i.e.* the first $M \leq N$ spatial modes capture more energy over the N snapshots than any other set of orthonormal spatial functions".

The first step of the snapshot method consists in the computation of the correlation matrix $\boldsymbol{C}$:

$$\boldsymbol{C}_{ij}=\sum_{k=1}^{P}\boldsymbol{u'}\left(\boldsymbol{x}_k,t_i\right)\boldsymbol{W}_{kk}\boldsymbol{u'}\left(\boldsymbol{x}_k,t_j\right), \boldsymbol{C}\in\mathbb{R}^{N\times N}, \boldsymbol{W}\in\mathbb{R}^{P\times P} \tag{2}$$

where $\boldsymbol{W}$ is a diagonal weighting matrix, for which the non-zeros elements are the cell volumes of each of the P grid points of one snapshot.

In the second step of the method, the temporal coefficients $a_m(t)$ are found using the solutions of the following eigenvalue problem:

$$\frac{1}{N}\sum_{j=1}^{N}\boldsymbol{C}_{ij}\alpha_m(t_j)=\lambda_m\alpha_m(t_i) \tag{3}$$

λ_m are eigenvalues and $\alpha_m(t)$ are eigenvectors of the correlation matrix. The eigenvalues are all real, with $\lambda_1 \geq \lambda_2 \geq ... \geq \lambda_N > 0$ and the eigenvectors $\alpha_m(t)$ are orthonormal. The temporal coefficients, $a_m(t)$, are a function of the eigenvectors and of the eigenvalues and they must be orthogonal:

$$a_m(t)=\sqrt{N\lambda_m}\alpha_m(t)\text{, with }\left\langle a_i\right\rangle_N=0\text{ and }\left\langle a_l a_m\right\rangle_N=\lambda_l\delta_{lm} \tag{4}$$

In the third step, the spatial modes are computed by projecting the fluctuating velocity ensemble onto the temporal coefficients, leading therefore to:

$$\boldsymbol{\phi}_m(\boldsymbol{x})=\frac{1}{N\lambda_m}\sum_{i=1}^{N}\boldsymbol{u'}(\boldsymbol{x},t_i)a_m(t_i)\text{, with }\left\|\boldsymbol{\phi}_m\right\|_{L^2}^2=\boldsymbol{\phi}_m^T\boldsymbol{W}\boldsymbol{\phi}_m=1 \tag{5}$$

The spatial modes are orthonormal with respect to the inner product in L^2, $\boldsymbol{\phi}_m{}^T\boldsymbol{W}\boldsymbol{\phi}_m$.

The mean fluctuating kinetic energy per unit mass captured by the m^{th} mode, E_m, finally writes:

$$E_m = \frac{1}{N}\sum_{i=1}^{N}\left\| a_m(t_i)\boldsymbol{\phi}_m(\boldsymbol{x})\right\|_{L^2}^2 = \frac{1}{N}\sum_{i=1}^{N} a_m(t_i)^2 = \lambda_m \tag{6}$$

while the mean total fluctuating kinetic energy per unit mass, E_T, is:

$$E_T = \sum_{m=1}^{N}\frac{1}{N}\sum_{i=1}^{N}\left\| a_m(t_i)\boldsymbol{\phi}_m(\boldsymbol{x})\right\|_{L^2}^2 = \sum_{m=1}^{N}\frac{1}{N}\sum_{i=1}^{N} a_m(t_i)^2 = \sum_{m=1}^{N}\lambda_m \tag{7}$$

3. EXPERIMENTAL SET-UP

3.1. Shallow rectangular reservoir

The experiments were carried out at the laboratory of engineering hydraulics of the University of Liege (ULg), Belgium. The experimental shallow reservoir is illustrated in Fig. 2; it consists in a 10.40 m long and 0.98 m wide horizontal channel, in which blocks can be rearranged to build different geometries of rectangular reservoirs.

The required discharge is injected in the upstream part of the flume, which is constituted by a stilling basin and a porous screen that stabilized the flow injection. After some meters, the flow is contracted to the width of the inlet channel, *b*, through a converging section. The inlet channel is 2.00 m long and has straight parallel walls. At the entrance of the reservoir, the flow suddenly expands to the width of the reservoir, $B=b+2\times\Delta B$. At the exit of the reservoir, the flow suddenly contracts to the outlet channel width, which is the same as in the inlet channel. The outlet channel is 1.50 m long and it ends with a tailgate and a free flow. All the surfaces are made of glass, except the bottom of the flume (PVC) and the converging section (metallic sheets).

The reservoir was fed with a constant discharge, Q, regulated through a pressure sensor mounted on the pump and an overflow system that enabled to keep constant the head at the entrance of the pump. The water depth, H, was measured using an ultrasonic probe and water variations in the reservoir did not exceed 2 mm (*i.e.* maximum 10% of H). The uncertainty on the flow inflow discharge was δQ = 0.025 L/s and the relative uncertainty on the water depth measurement was $\delta H/H$ = 1%.

In the present paper, we use a Cartesian coordinate system in which x, y and z are the longitudinal, lateral and vertical directions, respectively; x = 0 immediately downstream from the inlet channel and y = 0 at the right bank of the reservoir. z = 0 at the bottom of the reservoir.

3.2. Measurements of velocity fields

Given the experimental set-up and the size of the experiments, only the surface flow was reasonably accessible. The surface dynamics was therefore estimated using the surface velocity fields measured by Large-Scale PIV (LSPIV) and we assumed that it provides a reasonable representation of the large-scale instabilities. This assumption is supported by the results of Rowland *et al.* (2009), who showed in a configuration similar to ours (acrylic bed, $\mathsf{R} = 27000$, $H/B = 0.2$, with H constant in most part of the reservoir) that when approaching the free surface the characteristics of a jet in a confined layer almost corresponds to those of a self-similar plane-jet and comparisons between the mid-flow and surface measurements indicated very similar characteristics. Nevertheless, since the water depth in our experiments is smaller than the 5 cm of the experiment of Rowland *et al.* (2009), some bottom generated-turbulence affects the flow near the bottom ($z/H < 0.16$, z being the altitude with respect to the experiment bottom). In addition, Foss and Jones (1968) and Holdeman and Foss (1975) observed that in the near and middle fields of a bounded jet ($x/H < 10$), vertical secondary currents are generated by the inlet and affect the vertical distribution of velocity. In the far-field ($x/H > 10$), these secondary currents become dynamically passive. Based on our experimental set-up, it is however not possible to quantitatively estimate the relative weight of these different effects on the flow. In contrast, using numerical modelling, Peltier *et al.* (2013) and Mariotti *et al.* (2013) showed a remarkable agreement between the measured characteristics of the jet and those predicted by a depth-averaged flow model (based on the shallow water equations). This also suggests that the measured surface velocity fields are fairly representative of the mean flow and of the large-scale instabilities.

For each experiment, sawdust of 2 mm of mean diameter was placed on the surface of the flow and a region of 1 m², containing the entrance of the reservoir, was video recorded at a rate of 25 Hz during 6 min using a commercial video-camera (Canon© HD-HG20). After extraction from the video using ffmpeg (http://ffmpeg.org), correction and orthorectification of the images to be processed using Imagemagick (http://www.imagemagick.org), one pixel was equal to a square of 1 mm side. Using a LSPIV code based on the work of Hauet *et al.* (2008b) and Hauet (2009), the surface velocity fields were worked out on a square grid of 1 cm × 1 cm.

The flow direction and patterns were globally well captured. However, the theoretical uncertainty on the mean surface velocity is between 6% and 17%, depending on the tilt angle of the video-camera and on the position within the recorded images (Hauet *et al.* 2008a). The uncertainty is even higher on the instantaneous/fluctuating surface velocity fields.

As consequence, spurious vectors in the measurement fields were identified using a median filter (Westerweel 1994) and they were discarded. In the present experiments (see Tab. 1), the number of spurious vectors did not exceed 3% of the computed vectors. The resulting velocity fields were then processed using the Matlab function *smoothn*, described in Garcia (2010) for interpolating the missing values and for smoothing the velocity fields. The smoothing parameter was optimized using the generalized cross-validation method (Garcia 2010; Wahba 1990). The smoothing operated as a low-pass filter and therefore enabled to reduce the influence of high-frequency parasite motion within data. This procedure is of high importance for discriminating the contributions of the different turbulent structures present in the flow. Without low pass filtering, the parasite motions are too energetic and they lowered the contribution of the turbulent structures of interest.

3.3. Data set

According to Peltier *et al.* (2014), for shape factors, SF, smaller than 6.2 and Froude numbers, $\mathsf{F} = U_{in} / \sqrt{gH}$ (U_{in} the mean velocity at the inlet and g the gravity acceleration) greater than 0.21, the flows developing in shallow rectangular reservoirs are meandering. Therefore, in the present set of experiments, the width of the inlet/outlet channels, b, was set to 0.08 m; the sudden expansion width, ΔB, was set to 0.45 m and the length of the reservoir, L, was equal to 1 m, so that the resulting shape Factor, SF, equals 4.43. Four couples of discharge/water depth were then chosen, so that the corresponding Froude numbers were greater than 0.21 and the corresponding friction numbers at the inlet, $\mathsf{S} = f \Delta B / 8H$ (f the Darcy-Weisbach coefficient) (Chu *et al.* 1983), cover a broad range of values. The main flow characteristics are summarized in Tab. 1 and the Reynolds numbers, $\mathsf{R} = U_{in}D/\nu$ (D the hydraulic diameter at the inlet and ν the kinematic viscosity), are given for information. They confirm that the flows are turbulent, but they are hydro-dynamically smooth. For the slowest case (F), some viscous effects may be present as the depth-dependent Reynolds number is close to 1000 (minimum $Q/\nu/b$ = 1500) (Chen and Jirka 1997).

The friction number is used here as a shallowness parameter (Chu *et al.* 2004) and quantifies the effect of the confinement exerted by the water depth on the coherent structures developing in the reservoir. From a systematic parametric study, Peltier *et al.* (2014) revealed a strong dependence to S for the characteristic lengths and frequency of the meandering jet:

1. The wave length of the meandering is mostly proportional to the water depth at low S and at high S it is proportional to the product of the expansion width (ΔB) and of the friction coefficient.
2. The depth-normalised lateral spreading of the jet is almost proportional to the square root of the friction number, which indicates that the lateral spreading is significantly influenced by the water depth, revealing a vertical confinement occurring at high S (low water depth).
3. A damping of the meandering frequency is observed with increasing friction and/or decreasing water depth.

This parameter S was chosen to remain consistent with previous studies dealing with symmetric and asymmetric flows in shallow rectangular reservoirs (Dufresne *et al.* 2010a; Peltier *et al.* 2013). These flows are similar to cavity flows and the confinement exerted by the water depth on the recirculating patterns is well represented by the friction number (Babarutsi *et al.* 1989; Babarutsi *et al.* 1996).

The different types of friction regimes were named referring to the work of Chu *et al.* (2004). The flow-case F (S = 0.18) belongs to the frictional regime (the turbulence scale is mainly driven by the water depth), while the flow-case NF (S = 0.03) belongs to the non-frictional regime (the turbulence scale is mainly driven by the horizontal length-scale, *i.e.* the sudden expansion width ΔB). For sudden expansions, Chu *et al.* (2004) identified a transition regime for S in-between 0.05 and 0.1. In the case of meandering flows, Peltier *et al.* (2014) a confinement effect was observed from S = 0.07. As a consequence the flow case FT (S = 0.10), was called frictional close to transition and the flow case NFT (S = 0.06) was called non-frictional close to transition.

4. POD ANALYSIS

4.1. Energy

The POD analysis was performed for each experimental flow-case on N = 9000 snapshots (video-sequence of 6 min at 25 fps). 9000 eigenvalues λ_m, representing the mean fluctuating kinetic energy in the m^{th} modes, could then be deduced. The M eigenvalues are ranked in descending order and their values dramatically decrease as m increases. This suggests that, apart from a reduced number of energetic modes (corresponding to $m \leq 10$), all other modes reflect motions with little contribution to the overall flow pattern.

The mean total fluctuating kinetic energy (E_T, Eq. 7) was calculated for each flow-case and was displayed in Fig. 3(a). It normalised by the square of the inlet velocity $U_{in} = Q/(Hb)$ (see Tab. 1), which represents the total kinetic energy injected in the flume. The ratio E_T/U_{in}^2 increases between F and FT cases, as well as between FT and NFT cases. This corresponds to an increasing relative importance of the fluctuating velocity field, as the discharge gradually increases (see Tab. 1). By contrast, a decrease in E_T/U_{in}^2 appears between NFT and NF cases, which suggests that the mean flow pattern has a greater relative incidence in the energy budget and less intense vortices are developing in the flow.

The normalised distribution of the mean fluctuating kinetic energy between the modes confirms the previous hypothesis (Fig. 3(b)). The three first modes of the NF-case and FT-case have similar levels of relative energy, yet U^2_{in} is three times higher for NF. Regarding the shape of the distributions, similarities can be found between the flow-cases. Most of the energy is contained in the 10 first modes (60-80% of E_T) and between one or two “plateaus” can be distinguished in the distributions (modes 1-2 and modes 4-5). This suggests that at least one or two sizes of coherent structures are convected at a roughly constant velocity in the flow (Brevis and García-Villalba 2011; Rempfer and Fasel 1994). The third mode is not paired and represents an ensemble motion of the flow (Shim *et al.* 2013).

Comparisons between cases highlight that third mode mean fluctuating kinetic energy is between 22% and 30% of the first mode one. On the other hand modes 4 and 5 of F and NF are equal to 18% of the first mode, while they are only equal to 7% for FT and NFT. This difference indicates that structures related to modes 1 and 2 have a greater relative weight for the transition regime than for the two other regimes.

4.2. Temporal coefficients

In Fig. 4 the temporal coefficients deduced from the eigenvectors (Eq. 4) of the five first modes are displayed for each flow-case. The temporal coefficients of the first and second modes have similar patterns, but they are phase-shifted in time; this confirms the pairing of these modes. By contrast, although oscillations are observed for the other modes (for $m > 2$), their amplitudes are smaller and less regular. A phase-shift between two consecutive modes is not obvious.

The power spectrum densities (PSD) of the temporal coefficients were then worked out for extracting the harmonics of the jet. The PSD were smoothed using the periodogram method to facilitate the identification of the peaks (Welch 1967), therefore introducing uncertainties in the frequency of the peaks equal to 0.03-0.05 Hz. An example of PSD is displayed in Fig. 5(a) for the flow-case FT. The magnitude of the Peak decreases with increasing mode number and for m > 2 their identification is not easy, because of the flat magnitude of the signal at low frequency.

The estimated dominant frequencies of the hundred first temporal coefficients were plotted against the number of the mode in Fig. 5(b) for all flow-cases. Excepted for a very limited number of modes, most of the harmonics of the jet are measured for the twenty first modes, indicating that the remaining modes are rather random and have little incidence on the periodicity of the jet. Regarding the frequency values, those of the first two modes distinctively increase with the total discharge, but no clear tendency is observed between the modes for a given flow-case, *i.e.* the frequency does not monotonously decrease nor increase with increasing mode number. Finally, the frequency value for modes 4 and 5 definitively confirms the pairing of these modes.

4.3. Spatial modes

To distinguish the coherent structures in the spatial modes, we used the definition of a vortex given by Kolář (2007), *i.e.* the vortex region is characterized by non-zero residual vorticity when $|s|<|w|$ (s the 2D principal rate of strain and w the vorticity-tensor component in 2D). The residual vorticity, w_{res}, is expressed as follows:

$$w_{res} = \mathrm{sgn}(w)\left(|w| - |s|\right), \text{ with } w_{res} = 0 \text{ for } |s| \geq |w|$$
$$|s| = \sqrt{4\left(\frac{\partial \phi_{xm}}{\partial x}\right)^2 + \left(\frac{\partial \phi_{xm}}{\partial y} + \frac{\partial \phi_{ym}}{\partial x}\right)^2} \Big/ 2 \text{ and } w = \left(\frac{\partial \phi_{ym}}{\partial x} - \frac{\partial \phi_{xm}}{\partial y}\right) \Big/ 2 \tag{8}$$

where ϕ_{xm} (resp. ϕ_{ym}) is the longitudinal (resp. lateral) component of the m^{th} spatial mode.

The streamlines and the residual vorticity of the five first spatial modes computed with Eq. 5 are displayed in Fig. 6 for each flow-case. As a comparison with the work of Giger *et al.* (1991) and Dracos *et al.* (1992), the near field limit (x = 2H) and the middle-field limit (x = 10H) were represented in Fig. 6 by vertical dashed lines. According to Dracos *et al.* (1992), the flow behaves like a 2D plane jet in the near-field, the secondary currents observed by Foss and Jones (1968) then affect the jet in the middle field and finally the meandering flow pattern, associated to large vortices, appears in the far-field (x > 10H).

Comparisons between modes emphasize that the first and the second modes are systematically paired and space-shifted. This confirms that these modes characterize a size of coherent structures. The third mode for all cases represents a large pattern of very low frequency, which indicates that not only coherent structures significantly contribute to the flow energy. A pairing is also confirmed between modes 4 and 5 for the flow-cases close to the transition regime (FT and NFT). Above m = 5, a pairing may also be observed, but the percentage of the mean fluctuating kinetic energy contained in these modes (see in Fig. 3(b)), has little influence on the coherent motion of the flow.

Since the patterns of the spatial modes change with the friction number, they give an insight into the effect of shallowness on the development of the meandering jet. Regarding modes 1 and 2, little information is available in the near field of the jet (x < 2H). In the middle-field of the jet (2H < x < 10H), small symmetrical coherent structures relative to the reservoir centreline are systematically present in the frictional (F) and transition flow-cases (FT and NFT). For the non-frictional case (NF), they are only observed until x > 5H. The rotating direction of these structures alternates in the streamwise direction. In the far field of the jet, the distance for which the counter-rotating symmetrical structures are still observed, increases with the friction number (Tab. 2). Downstream from this distance, they merge into larger counter-rotating vortices centred on the centreline reservoir. The size of these large structures increases with a decreasing friction number for

0.18 < S < 0.06. For S = 0.03 (NF), the size is smaller than in the NFT flow-case, which is consistent with the observation on the energy in paragraph 4.1. The loss in energy and size of the structure may be due to a lateral confinement operated by the reservoir lateral walls, which prevents the structures to laterally spread and therefore increases the dissipation of the fluctuating energy. The pattern of mode 3 does not reveal the existence of coherent structures. Finally, modes 4 and 5 show antisymmetric vortices relative to the reservoir centreline for F, FT and NFT in most part of the reservoir. For the NF-case, distinctive patterns cannot be identified, except in the far-field of mode 5. As for the symmetric vortices of modes 1 and 2, the antisymmetric vortices are counter-rotating in the streamwise direction.

5. COHERENT STRUCTURES

The POD analysis enables to characterise the energy distribution between the different modes, but it gives little information on how the different structures cohabit in the jet. Therefore, a specific analysis has been undertaken to identify these coherent structures.

5.1. Reconstruction of the velocity fields

As shown in Fig. 7(a) for flow-case FT, the fluctuating velocity fields directly deduced from the raw data contain high frequency motions, which make it more difficult to identify the coherent structures present in the meandering jet. These parasite motions can be filtered using the results of the POD modes and Eq. 1.

For this purpose, the velocity fields were reconstructed using the POD modes, which contribute the most to the coherent motion in terms of energy, the remaining modes being omitted/filtered. The choice of the number of modes, *M*, is a key parameter in such a reconstruction (Perrin *et al.* 2007). Taking a too large *M* number would lead (1) to an overestimation of the contribution of the coherent motion to the flow and (2) to the reintroduction of high frequency motions. As noticed by Perrin *et al.* (2007) in the near wake of a circular cylinder, the choice of *M* must be related to the fundamental frequency of the vortex shedding in the flow. Above a certain number of modes *m*, if the harmonics of the phenomenon are not clearly observed in the temporal coefficients, or if the energy of the considered modes is too low, the remaining modes may be assumed to have low influence on the coherent motion and therefore, they should not be considered in the reconstruction process.

In this study, in addition to the presence of the harmonics of the jet, the choice of the number of modes for reconstructing the fluctuating velocity fields was also based on the amount of energy contained in each mode and we also evaluate the ability of the reconstruction to reproduce the cross-product distribution, $-u'v'$, within the jet. The cross-product is indeed an indicator of the presence of coherent structures in the flow.

In Fig. 7(b), a fluctuating velocity field for flow-case FT was reconstructed using the two first modes: the matching between the raw data (Fig. 7(a)) and the reconstructed field is not satisfactory. Most of the structures present in the jet are represented, but the shapes are not consistent. The same observations are made regarding the cross-product distribution, where the levels are not recovered. For flow-case FT, although the first two modes contain 50% of the mean total fluctuating kinetic energy, they do not contain all the harmonics of the jet (Fig. 5(b)). More modes need therefore to be taken into account in the reconstruction of the velocity field. In Fig. 7(c), the fluctuating velocity field was then reconstructed using the modes containing the main harmonic of the jet (Fig. 5(b)) plus some additional modes to reach 80% of the mean total fluctuating kinetic energy. With respectively $M = 59$ for F, $M = 16$ for FT, $M = 10$ for NFT and $M = 33$ for NF, the main flow patterns are well described, the parasite motions being still filtered and the cross-product distributions are matching.

Seven transversal profiles of the cross-product, $-u'v'$, for the raw and of the reconstructed velocity fields are displayed in Fig. 8 for each flow-case. The comparison of both reconstructions emphasizes that the one using the modes containing 80% of the mean total fluctuating kinetic energy is the most efficient reconstruction, whether close to the inlet or close to the outlet. The flow patterns in the jet are indeed well represented and most of the parasite motions outside of the jet are filtered.

5.2. Identification of coherent structures

As shown in section 4.3 for spatial modes, the coherent structures in the reconstructed fields can be identified by applying Eq. 8 on the reconstructed velocity fields (replace respectively ϕ_{xm} and ϕ_{ym} by u' and v' in Eq. 8). As a result, as soon as a coherent structure is present in the flow, the residual vorticity is non-zero. Nevertheless, the identification of the structures' extent / shape in each individual snapshot strongly depends on the method of extraction (circulation calculation, vorticity threshold) and could lead to erroneous identification. Therefore, the characterisation of the coherent structures in the flow were based here on a more effective approach that only considers the centres of the coherent structures and the time-evolution of the positions of these centres in the reservoir. It relies on the assumption of quasi-circular vortices, which is found reasonable here. Indeed, for each experiment, the calculation of the residual vorticity highlights that most structures in the flow are almost circular in shape and are distributed either on the reservoir centreline or on both sides of it (Fig. 9).

The centres of the structures in the meandering jet were detected using a topology algorithm similar to the method developed by Depardon *et al.* (2006). This algorithm detects the nodes, the focuses (*i.e.* the vortex centre) and the saddles in the flow. As an example of the calculation, the computed centres are superimposed to the residual vorticity (Eq. 8) in Fig. 9 for each flow-case. The centres satisfactorily match with the maxima of residual vorticity, even if these maxima are not close to the centreline of the reservoir: the computed focuses successfully locate the coherent structure centres.

The topology calculation was performed over 500s to determine the "trajectories" of the coherent structures in the flow between $x = 0$ m and $x = 0.7$ m (after 0.7 m, the computation failed because of the lack of data in the blank zone, see Fig. 1). The results are presented in Fig. 10 every 0.2s and the x-axis was normalised by the respective mean water depth in the reservoir to identify the near ($x/H < 2$), middle ($2 < x/H < 10$) and far ($x/H > 10$) fields for bounded jets (Dracos *et al.* 1992). The positions of the centres indicate that in the near field of the jet, all the coherent structures are paired and counter-rotating. Moreover, given the sign of the residual vorticity in Fig. 9, these structures are symmetric. In the middle and far fields, the distance at which the symmetrical counter-rotating structures merge reduces with a decreasing friction number (F to NF). This reveals a dependence of the coherent structures on the shallowness. This is consistent with a weakening, with decreasing friction number, of the bounding effect operated by the vertical secondary flows in the middle field (Foss and Jones 1968; Holdeman and Foss 1975). The distances of appearance of large structures correspond with the distances in Tab. 2, which indicate that in the contrary of what was observed by Dracos *et al.* (1992) the middle-far field limit is not always located at x/H = 10. This difference in the structure development is due to a larger influence of the geometric aspect-ratio in our experiments. The shallowness is indeed higher in the present experiments ($H/b \in [0.16 - 0.53]$, with b = 8 cm) than in the work of Dracos *et al.* (1992) for which $H/b \in [2 - 36]$ (with b = 1 cm).

The study of the trajectories of the centres finally indicates that the symmetric counter-rotating structures are relatively stable in time. By contrast, the variability in time of the large coherent structures clearly depends on the position within the jet. In the middle field, the trajectories of the coherent structures are quite stable, while a clear dependence in time is observed in the far field. For the frictional case (F), the trajectories are stable. For the transition-cases (FT and NFT), the motion of the structures is particularly slow, while for the non-frictional case (NF) the trajectories indicate a quicker motion of the structures. These results finally emphasize that when the friction number, S, decreases, the small and stable in time counter-rotating structures developing on both sides of the centreline of the reservoir degenerate into larger structures, which centres periodically oscillates around the reservoir centreline.

6. STABILITY CONSIDERATIONS

The coherent structures convectively displaced within the jet towards the reservoir exit appear as a result of flow instabilities. The shape of the paired modes can be related to the varicose and sinuous instability modes (Thomas and Prakash 1991). On the one hand, the alternative succession of negative and positive vortical structures along the reservoir centreline in the modes 1 and 2 is responsible for the meandering of the jet and are characteristics of the sinuous mode of the jet (Söderberg and Alfredsson 1998, Lombardi, 2011 #1047; Thomas and Prakash 1991). On the other hand, the antisymmetric counter-rotating structures on both sides of the centreline for modes 4 and 5 are characteristics of the varicose mode and are responsible for a local mixing (Shim *et al.* 2013). Moreover given the relative weight of modes 1 and 2 compared to the others (Fig. 3), the sinuous mode is dominant in each flow-case.

Socolofsky and Jirka (2004) refer to instability modes as absolutely unstable (small perturbations grow at a fixed point above a certain threshold) or convectively unstable (small perturbations grow at a moving point above a certain threshold). Among other authors Chen and Jirka (1998) and Socolofsky and Jirka (2004) characterised the stability of a jet by proceeding to a linear stability analysis of the shallow water equations considering no lateral confinement and the standard hyperbolic jet profile:

$$\langle \boldsymbol{u}(x,y,t)\rangle_N = \bar{u}\left[1-R_u+2R_u\,\mathrm{sech}^2\left(\frac{0.881\times(y-y_c)}{b_{1/2}}\right)\right],\ \text{with } R_u=\frac{u_c-u_\infty}{u_c+u_\infty} \text{ and } \bar{u}=\frac{u_c+u_\infty}{2} \qquad (9)$$

u_c being the centreline velocity, y_c the lateral coordinate of the centreline and u_∞ the ambient flow velocity. They also defined a stability number, $\mathsf{S}_j = fb_{1/2}/4H$, for jet flows using the half-width of the jet, $b_{1/2}$ as characteristic length. As a result, Chen and Jirka (1998) found that for a pure jet (R_u = 1), the varicose mode is stable when $\mathsf{S}_j > 0.11$ and the sinuous mode is stable for $\mathsf{S}_j > 0.685$. In the sequel, Socolofsky and Jirka (2004) proceeded to some correction of the equations used by Chen and Jirka (1998) and found that the stabilizing effect of the bottom friction was underestimated. The correction was applied on the sinuous mode, the critical stability number of which becoming equal to 0.6 for R_u = 1; below the critical value, the flow is convectively unstable, above, the flow is stable. They also found that the critical stability number increases with R_u and from $R_u > 1.2$, the jet cannot be stable. They finally indicate that from R_u = 1.6 and $\mathsf{S}_j = 0$, the instability is absolute.

In the present experiments, we followed the recommendations of Socolofsky *et al.* (2003) for computing a stability number as a function of the streamwise distance in order to evaluate the streamwise evolution of the instabilities. $b_{1/2}$ was calculated for each streamwise position using the definition of Rowland *et al.* (2009): $b_{1/2}$ corresponds to the lateral position, where the velocity is equal to the half of the centreline velocity. The ambient velocity was estimated by solving Eq. 9 in order to have the best fit of the lateral velocity profiles of $\langle \boldsymbol{u}(x,y,t)\rangle_N$ and R_u was therefore estimated. The stability number is displayed as a function of R_u in Fig. 11(a), showing that the flow fields considered here are all unstable. The F and FT cases are convectively unstable everywhere in the reservoir. By contrast the NFT and NF-case become absolutely unstable close to the exit of the reservoir (see the values of R_u in Fig. 11(b)). This could explain the more variable trajectories (in space and time) of the centres of NFT and FT at the end of the reservoir (Fig. 10(c-d)).

Ghidaoui *et al.* (2006) revealed the existence of secondary instabilities in the flow, because of the presence of additional inflection points in the velocity profile due to a lateral bounding effect of the lateral wall. Nevertheless given the dominance of the two first modes on the meandering jet, these secondary instabilities have probably limited effects in the present case.

7. CONCLUSION

The present paper investigates four meandering flows in a shallow rectangular reservoir. The reservoir boundary conditions were set-up so that the flows significantly differed in term of friction number. The flow dynamics was measured using LSPIV and the resulting velocity fields were corrected using a median-filter and a smoothing algorithm.

With the objective of characterising the influence of the shallowness of the flow on the coherent structures developing within the jet, a POD analysis was first performed on the fluctuating velocity fields to discriminate the structures in terms of their relative contributions to the mean total fluctuating kinetic energy. It results that amongst the 9000 computed POD modes, only few modes really contribute to the coherent motions, the remaining modes being only parasite motions or high frequency motions. The study of the POD modes reveals the presence of three types of coherent structures. In the two first modes, small symmetric counter-rotating structures first develop in the flow and then merge into large coherent counter-rotating structures. The meandering of the jet is due to these structures. The structures in the other modes are antisymmetric and counter-rotating and have little influence on the meandering.

The characteristics of the coherent structures were obtained using the residual vorticity and a topology algorithm for extracting the centre of these structures. As parasite and high frequency motions were present on the raw fluctuating velocity fields, fluctuating velocity fields without these motions were obtained by velocity reconstruction using the POD modes containing 80% of the mean total fluctuating kinetic energy. Only two types of structures were identified confirming the dominance of the two first POD modes. Small symmetric counter-rotating coherent structures first develop on both sides of the centreline of the reservoir. Then, they merge into large coherent structures, the centres of which are located on the centreline. These large structures gradually grow until the end of the reservoir. The study of the trajectories of the centres indicates that the size of the coherent structures strongly depends on the friction number. At high friction number, small structures are mainly observed, therefore indicating that the vertical confinement operated by the water depth prevents the coherent structures from laterally spreading. By contrast, at low friction number, the large structures are almost present from the beginning of the reservoir: the separation of the flow into near, middle and far fields is not appropriate for such flows. The shallowness of the flow indeed affects the position, where the small paired structures merge into large structures.

Finally, the comparison with the literature on the onset to instability reveal that two instability modes are involved in the jet (sinuous *vs.* varicose). The sinuous mode is largely dominant and is responsible for the meandering of the jet. In each experiment, the sinuous mode is convectively unstable and tends to become absolutely unstable at the end of the reservoir for low friction number.

8. ACKNOWLEDGMENTS

The research was funded by the University of Liège (grant SFRD-12/27). The authors are grateful for the assistance provided by the research technicians during the experiments and the fruitful discussions about the POD analysis with Professor Vincent Denoël. The authors are thankful to the two anonymous reviewers, whose remarks allow a substantial improvement of the present work.

9. REFERENCES

Aloui F, Souhar M (2000) Experimental study of turbulent asymmetric flow in a flat duct symmetric sudden expansion. Journal of Fluids Engineering, Transactions of the ASME 122:174-177

Babarutsi S, Ganoulis J, Chu VH (1989) Experimental investigation of shallow recirculating flows. Journal of Hydraulic Engineering, ASCE 115(7):906-924

Babarutsi S, Nassiri M, Chu VH (1996) Computation of shallow recirculating flow dominated by friction. Journal of Hydraulic Engineering, ASCE 122:367-372

Berkooz G, Holmes P, Lumley JL (1993) The proper orthogonal decomposition in the analysis of turbulent flows. Annual Review of Fluid Mechanics 25:539-575

Brevis W, García-Villalba M (2011) Shallow-flow visualization analysis by proper orthogonal decomposition. Journal of Hydraulic Research 49:586-594 DOI 10.1080/00221686.2011.585012

Camnasio E, Erpicum S, Orsi E, Pirotton M, Schleiss AJ, Dewals B (2013) Coupling between flow and sediment deposition in rectangular shallow reservoirs. Journal of Hydraulic Research DOI 10.1080/00221686.2013.805311

Camnasio E, Orsi E, Schleiss AJ (2011) Experimental study of velocity fields in rectangular shallow reservoirs. Journal of Hydraulic Research 49:352-358

Canbazoglu S, Bozkir O (2004) Analysis of pressure distribution of turbulent asymmetric flow in a flat duct symmetric sudden expansion with small aspect ratio. Fluid Dynamics Research 35:341-355

Canestrelli A, Nardin W, Edmonds D, Fagherazzi S, Slingerland R (2014) Importance of frictional effects and jet instability on the morphodynamics of river mouth bars and levees. Journal of Geophysical Research: Oceans:n/a-n/a DOI 10.1002/2013JC009312

Chen D, Jirka GH (1997) Absolute and convective instabilities of plane turbulent wakes in shallow water layer. Journal of Fluid Mechanics 338:157-172

Chen D, Jirka GH (1998) Linear stability analysis of turbulent mixing layers and jets in shallow water layers. Journal of Hydraulic Research 36:815-830

Chu VH, Khayat RE, Wu JH (1983) Stability of turbulent shear flows in shallow channel 20th IAHR Congr, Sep 5-9, Moscow, USSR. Delft, The Netherlands, IAHR, pp. 128-133

Chu VH, Liu F, Altai W (2004) Friction and confinement effects on a shallow recirculating flow. Journal of Environmental Engineering and Science 3:463-475 DOI 10.1139/S04-034

Couplet M, Sagaut P, Basdevant C (2003) Intermodal energy transfers in a proper orthogonal decomposition - Galerkin representation of a turbulent separated flow. Journal of Fluid Mechanics:275-284

Depardon S, Lasserre JJ, Brizzi LE, Borée J (2006) Instantaneous skin-friction pattern analysis using automated critical point detection on near-wall PIV data. Measurement Science and Technology 17:1659-1669

Dewals BJ, Kantoush SA, Erpicum S, Pirotton M, Schleiss AJ (2008) Experimental and numerical analysis of flow instabilities in rectangular shallow basins. Environmental Fluid Mechanics 8:31-54

Dracos T, Giger M, Jirka GH (1992) Plane turbulent jets in a bounded fluid layer. Journal of Fluid Mechanics 241:587-614

Dufresne M, Dewals B, Erpicum S, Archambeau P, Pirotton M (2012) Flow patterns and sediment deposition in rectangular shallow reservoirs. Water and Environment Journal

Dufresne M, Dewals BJ, Erpicum S, Archambeau P, Pirotton M (2010a) Classification of flow patterns in rectangular shallow reservoirs. Journal of Hydraulic Research 48:197-204

Dufresne M, Dewals BJ, Erpicum S, Archambeau P, Pirotton M (2010b) Experimental investigation of flow pattern and sediment deposition in rectangular shallow reservoirs. International Journal of Sediment Research 25:258-270

Dufresne M, Dewals BJ, Erpicum S, Archambeau P, Pirotton M (2011) Numerical investigation of flow patterns in rectangular shallow reservoirs. Engineering Applications of Computational Fluid Mechanics 5:247-258

Foss JF, Jones JB (1968) Secondary Flow Effects in a Bounded Rectangular Jet. Journal of Basic Engineering 90:241-248 DOI 10.1115/1.3605085

Garcia D (2010) Robust smoothing of gridded data in one and higher dimensions with missing values. Computational Statistics & Data Analysis 54:1167-1178 DOI 10.1016/j.csda.2009.09.020

Ghidaoui MS, Kolyshkin AA, Liang JH, Chan FC, Li Q, Xu K (2006) Linear and nonlinear analysis of shallow wakes. Journal of Fluid Mechanics 548:309-340 DOI 10.1017/S0022112005007731

Giger M, Dracos T, Jirka GH (1991) Entrainment and mixing in plane turbulent jets in shallow water. Journal of Hydraulic Research 29:615-642

Graftieaux L, Michard M, Nathalie G (2001) Combining PIV, POD and vortex identification algorithms for the study of unsteady turbulent swirling flows. Measurement Science and Technology 12:1422-1429

Guo B, Langrish AG, Fletcher DF (1998) Time-dependent simulation of turbulent flows in axisymmetric sudden expansions 13th Australian Fluid Mechanics Conference. Monash University, Melbourne, Australia, pp. 283-286

Hauet A (2009) Discharge estimate and velocity measurement in river using Large-Scale Particle Image Velocimetry; Estimation de débit et mesure de vitesse en rivière par Large-Scale Particle image Velocimetry. La Houille Blanche:80-85 DOI 10.1051/lhb.2009009

Hauet A, Creutin JD, Belleudy P (2008a) Sensitivity study of large-scale particle image velocimetry measurement of river discharge using numerical simulation. Journal of Hydrology 349:178-190 DOI 10.1016/j.jhydrol.2007.10.062

Hauet A, Kruger A, Krajewski WF, et al. (2008b) Experimental system for real-time discharge estimation using an image-based method. Journal of Hydrologic Engineering 13:105-110 DOI 10.1061/(ASCE)1084-0699(2008)13:2(105)

Holdeman JD, Foss JF (1975) The Initiation, Development, and Decay of the Secondary Flow in a Bounded Jet. Journal of Fluids Engineering 97:342-352 DOI 10.1115/1.3447313

Holmes P, Lumley JL, Berkooz G, Rowley CW (2012) Turbulence, Coherent Structures, Dynamical Systems and Symmetry. Second Edition. Cambridge University Press,

Honeyands TA, Molloy AA (1995) Oscillations of submerged jets confined in a narrow deep rectangular cavity 12th Australian Fluid Mechanics Conference. the University of Sydnay, Australia, pp. 493-496

Kantoush SA, De Cesare G, Boillat JL, Schleiss AJ (2008) Flow field investigation in a rectangular shallow reservoir using UVP, LSPIV and numerical modelling. Flow Measurement and Instrumentation 19:139-144

Khan S, Melville BW, Shamseldin AY, Fischer C (2013) Investigation of flow patterns in storm water retention ponds using CFD. Journal of Environmental Engineering (United States) 139:61-69

Kolář V (2007) Vortex identification: New requirements and limitations. International Journal of Heat and Fluid Flow 28:638-652

Landel JR, Caulfield CP, Woods AW (2012) Meandering due to large eddies and the statistically self-similar dynamics of quasi-two-dimensional jets. Journal of Fluid Mechanics 692:347-368 DOI 10.1017/jfm.2011.518

Lawson NJ, Davidson MR (2001) Self-sustained oscillation of a submerged jet in a thin rectangular cavity. Journal of Fluids and Structures 15:59-81

Mariotti G, Falcini F, Geleynse N, Guala M, Sun T, Fagherazzi S (2013) Sediment eddy diffusivity in meandering turbulent jets: Implications for levee formation at river mouths. Journal of Geophysical Research F: Earth Surface 118:1908-1920 DOI 10.1002/jgrf.20134

Mullin T, Shipton S, Tavener SJ (2003) Flow in a symmetric channel with an expanded section. Fluid Dynamics Research 33:433-452

Oca J, Masaló I (2007) Design criteria for rotating flow cells in rectangular aquaculture tanks. Aquacultural Engineering 36:36-44

Peltier Y, Erpicum S, Archambeau P, Pirotton M, Dewals B (2013) Experimental and numerical investigation of meandering jets in shallow reservoir: potential impacts on deposit patterns. In: Nguyen KD, Benoit M, Guillou S, Sheibani N, Philipps JG and Pham Van Bang D (eds) THESIS 2013, Two-pHase modElling for Sediment dynamIcs in Geophysical Flows. SHF - EDF R&D, Chatou, France,

Peltier Y, Erpicum S, Archambeau P, Pirotton M, Dewals B (2014) Experimental investigation of meandering jets in shallow reservoir. Environmental Fluid Mechanics DOI DOI 10.1007/s10652-014-9339-2

Peng Y, Zhou JG, Burrows R (2011) Modeling free-surface flow in rectangular shallow basins by using lattice boltzmann method. Journal of Hydraulic Engineering 137:1680-1685

Perrin R, Braza M, Cid E, et al. (2007) Obtaining phase averaged turbulence properties in the near wake of a circular cylinder at high Reynolds number using POD. Experiments in Fluids 43:341-355

Rempfer D, Fasel HF (1994) Evolution of three-dimensional coherent structures in a flat-plate boundary layer. Journal of Fluid Mechanics 260:351-375

Rowland JC, Stacey MT, Dietrich WE (2009) Turbulent characteristics of a shallow wall-bounded plane jet: Experimental implications for river mouth hydrodynamics. Journal of Fluid Mechanics 627:423-449 DOI 10.1017/S0022112009006107

Shim YM, Sharma RN, Richards PJ (2013) Proper orthogonal decomposition analysis of the flow field in a plane jet. Experimental Thermal and Fluid Science 51:37-55 DOI http://dx.doi.org/10.1016/j.expthermflusci.2013.06.014

Sirovich L (1987) Turbulence and the dynamics of coherent structures. PART I: coherent structures. Quarterly of Applied Mathematics 45:561-570

Socolofsky SA, Jirka GH (2004) Large-scale flow structures and stability in shallow flows. Journal of Environmental Engineering and Science 3:451-462 DOI 10.1139/S04-032

Socolofsky SA, Von Carmer CF, Jirka GH (2003) Shallow turbulent wakes: linear stability analysis compared to experimental data. 1st IAHR International Symposium on Shallow Flows. A. A. Balkema Publishers, Delft, Netherlands, pp. 133-140

Söderberg LD, Alfredsson PH (1998) Experimental and theoretical stability investigations of plane liquid jets. European Journal of Mechanics, B/Fluids 17:689-737

Stovin VR, Saul AJ (2000) Computational fluid dynamics and the design of sewage storage chambers. Journal of the Chartered Institution of Water and Environmental Management 14:103-110

Thomas FO, Prakash KMK (1991) An experimental investigation of the natural transition of an untuned planar jet. Physics of Fluids A: Fluid Dynamics (1989-1993) 3:90-105 DOI doi:http://dx.doi.org/10.1063/1.857867

Wahba G (1990) Estimating the smoothing parameter. Spline Models for Observational Data. Society for Industrial Mathematics, Philadelphia, USA, pp. 45-65

Welch PD (1967) The use of Fast Fourier Transform for the estimation of power spectra: a method based on time-averaging over short, modified periodograms. Reprinted from IEEE, transactions of Audio and Electroacoustics AU15:70-73

Westerweel J (1994) Efficient detection of spurious vectors in particle image velocimetry data. Experiments in Fluids 16:236-247

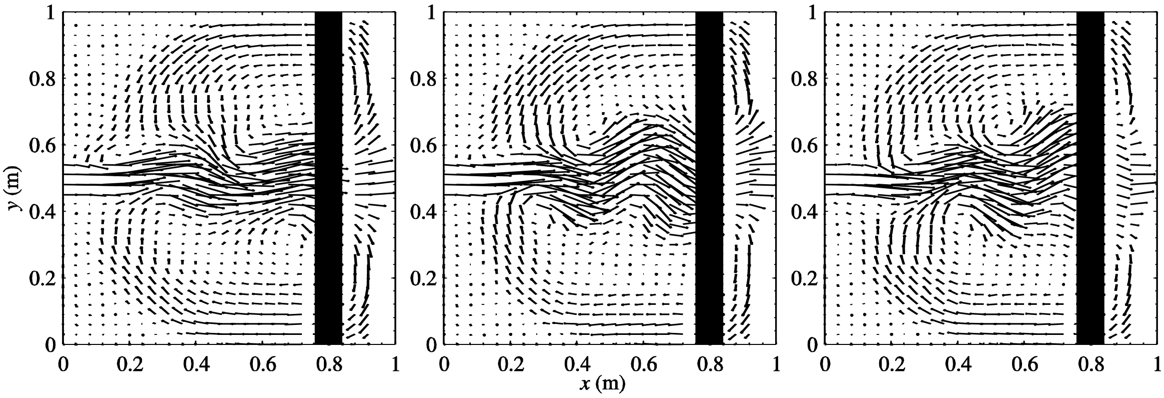

Fig. 1. Instantaneous velocity field at three instants (0s, 4s, 6s). The black rectangle corresponds to a blank zone during the measurement.

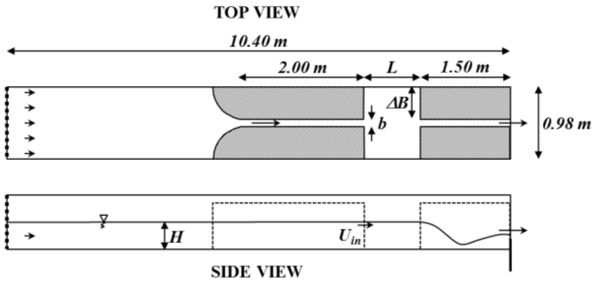

Fig. 2. Sketches of the experimental device (Peltier *et al.* 2014)

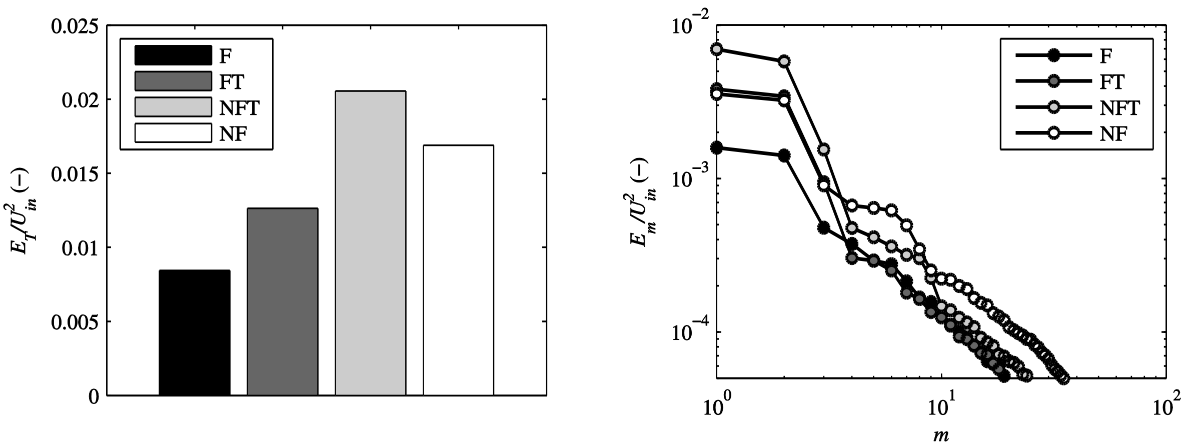

(a) (b)

Fig. 3. (a) Mean total fluctuating kinetic energy, E_T, normalised for each flow-case by their corresponding mean kinetic energy at the inlet (U^2_{in}). (b) Mean fluctuating kinetic energy contained in the m^{th} mode, E_m, normalised by U^2_{in}.

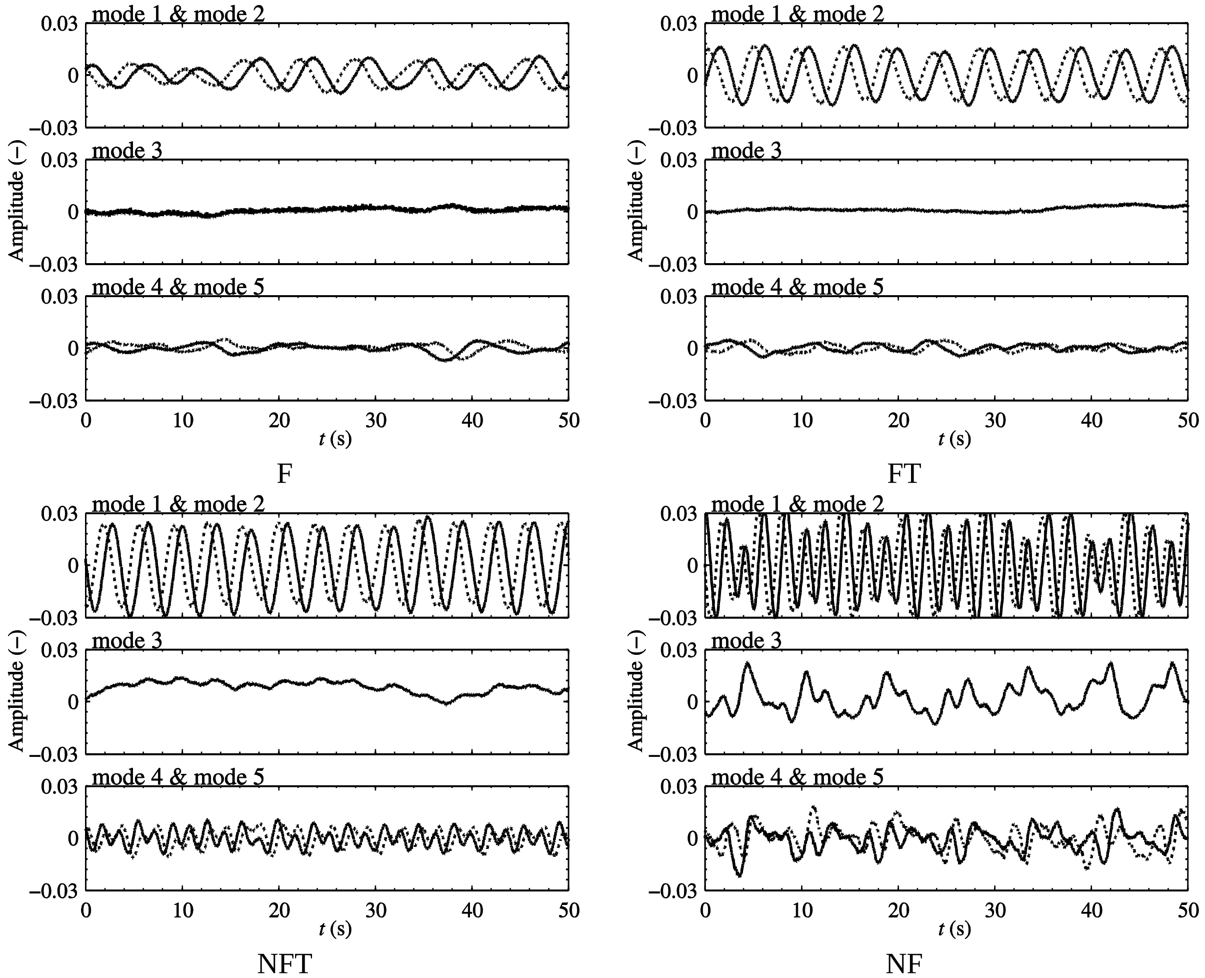

Fig. 4. Temporal coefficients of the five first mode of the POD analysis. The plain lines correspond to odd modes and the dotted lines to even modes.

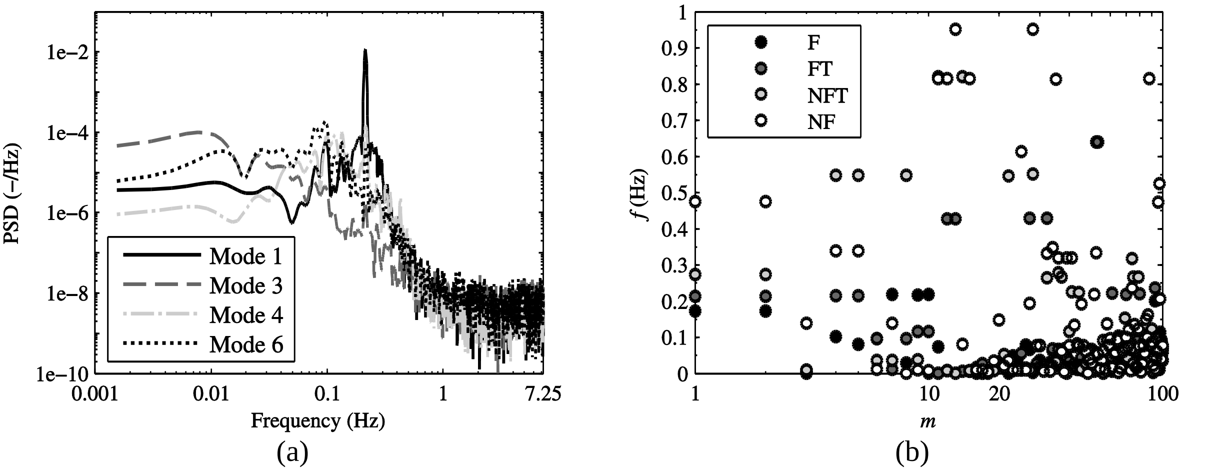

Fig. 5. (a) Power spectrum density (PSD) of four temporal coefficients for flow-case FT. (b) Frequencies of the temporal coefficients as a function of the number of the POD mode for each flow-case. Uncertainty of the frequencies: ±0.03-0.05 Hz.

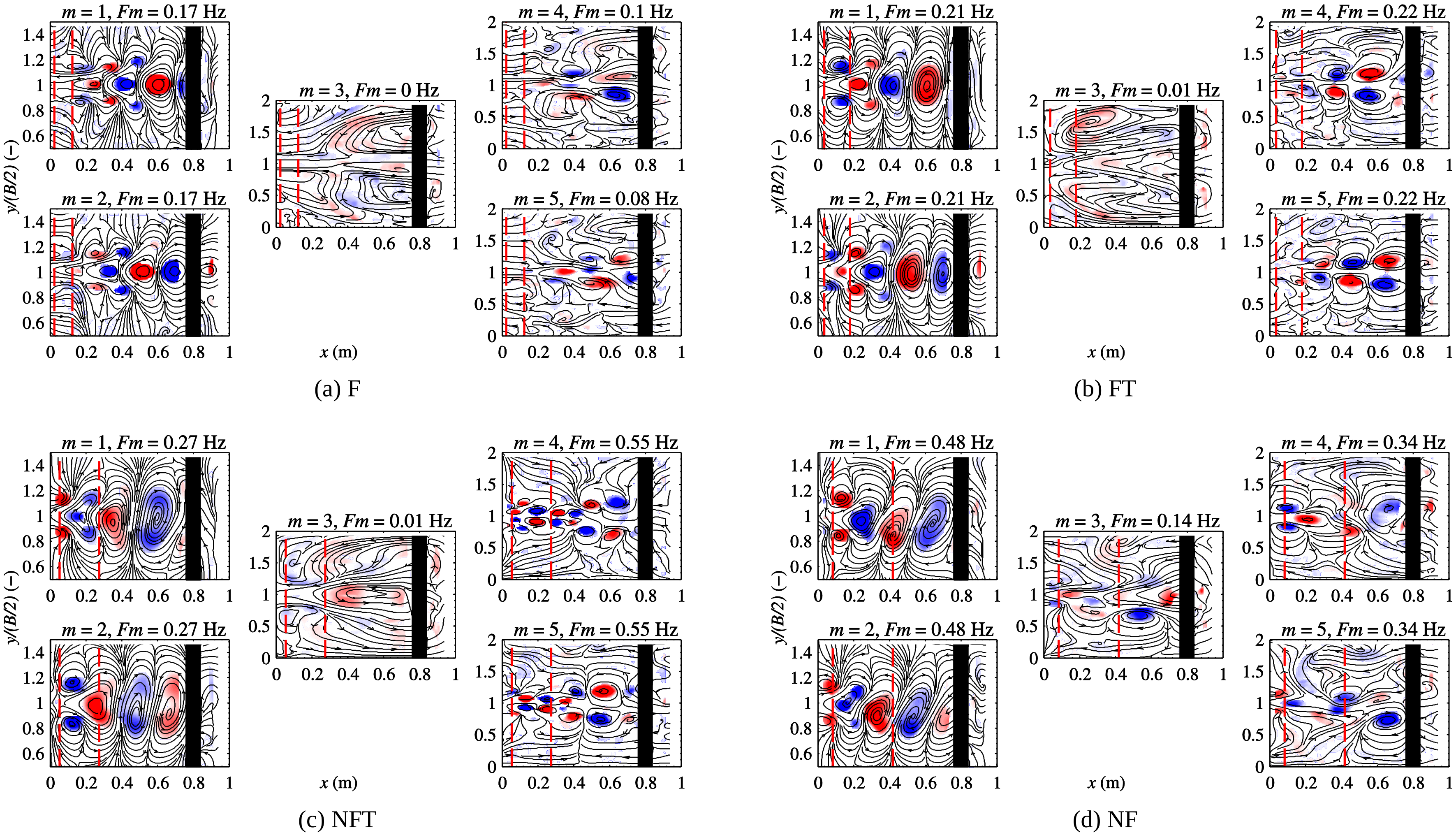

Fig. 6. Residual vorticity contours and streamlines of the 5 first spatial modes. The same colour-scale is used for all flow-cases (blue: vorticity < 0, white: vorticity = 0, red: vorticity > 0) and the colour intensity is proportional to the vorticity intensity. The black rectangle corresponds to a blank zone during the measurement. The vertical dashed lines correspond to *x/H* = 2 (limit between the near-field and the middle-field of the jet) and *x/H* = 10 (limit between the middle-field and the far-field of the jet).

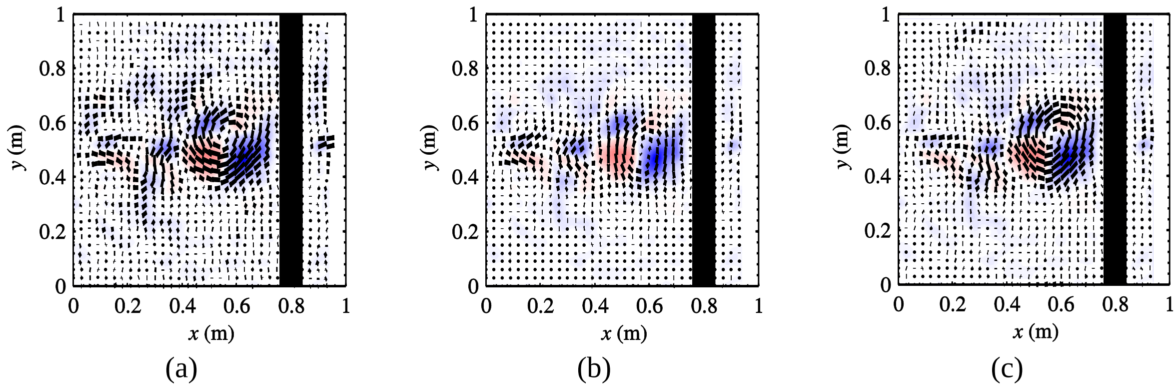

Fig. 7. Contour plot of normalised cross-product $-u'v'/U^2_{in}$ and fluctuating velocity field for flow-case FT. (a) Raw data. (b) Reconstructed data with $M = 2$. (c) Reconstructed data with the M first modes corresponding to 80% of E_T.

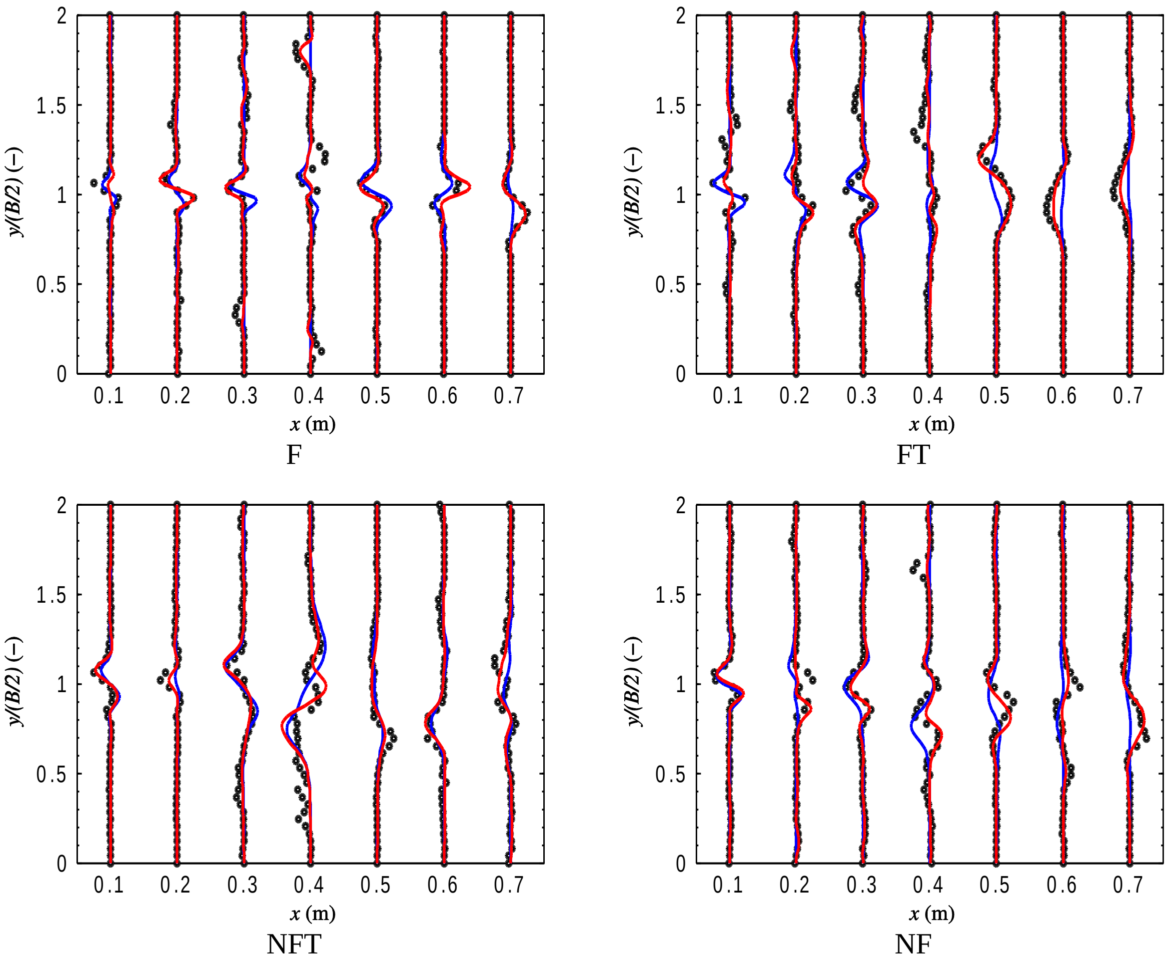

Fig. 8. Transversal profiles of the cross-product, $-u'v'$, for the raw data (o) and for the reconstructed velocity fields. (blue line) reconstruction with two modes, (red line) reconstruction with the M modes corresponding to 80% E_T (M = 59 for F, M = 16 for FT, M = 10 for NFT and M = 33 for NF).

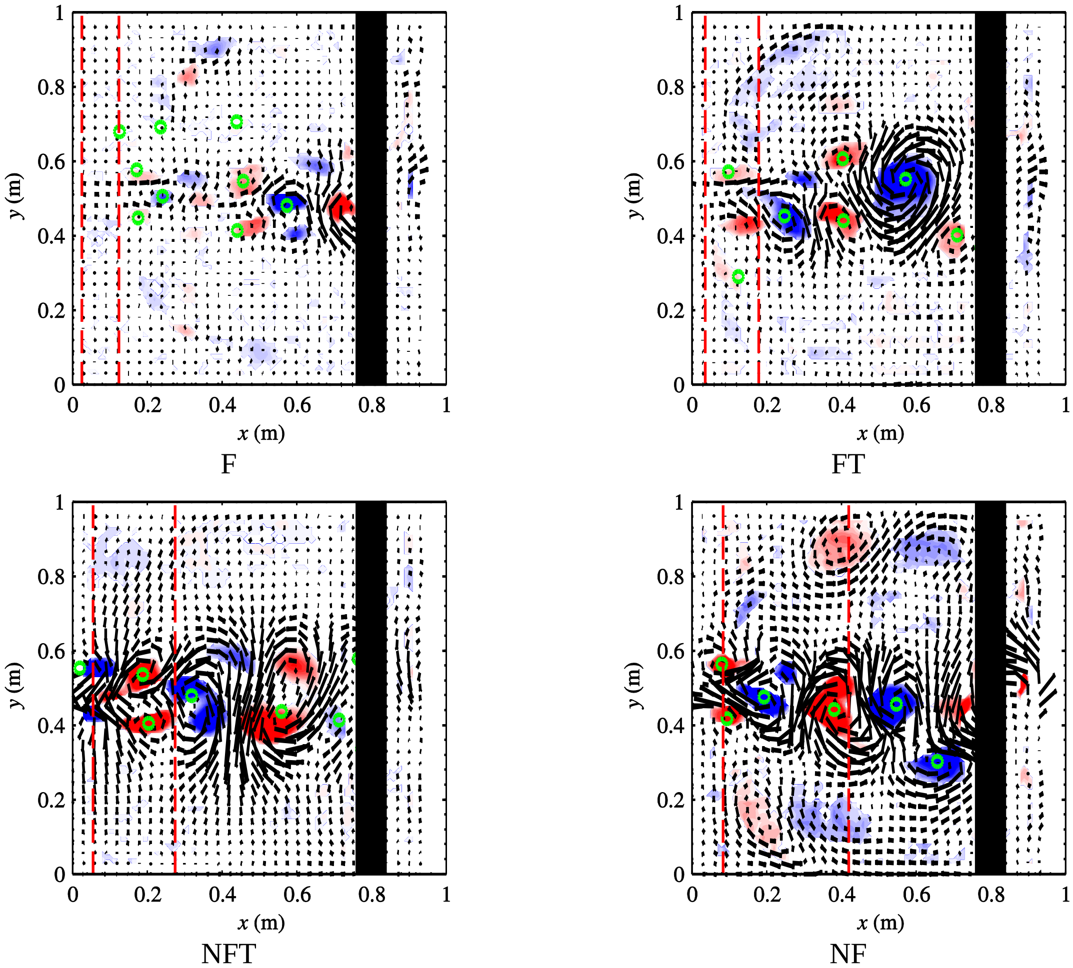

Fig. 9. Contour plot of residual vorticity (Eq. 8) and reconstructed fluctuating velocity field at 4 s. The circles localise the centre of the structures calculated with the topology algorithm. The vertical dashed lines correspond to *x/H* = 2 (limit between the near-field and the middle-field of the jet) and *x/H* = 10 (limit between the middle-field and the far-field of the jet).

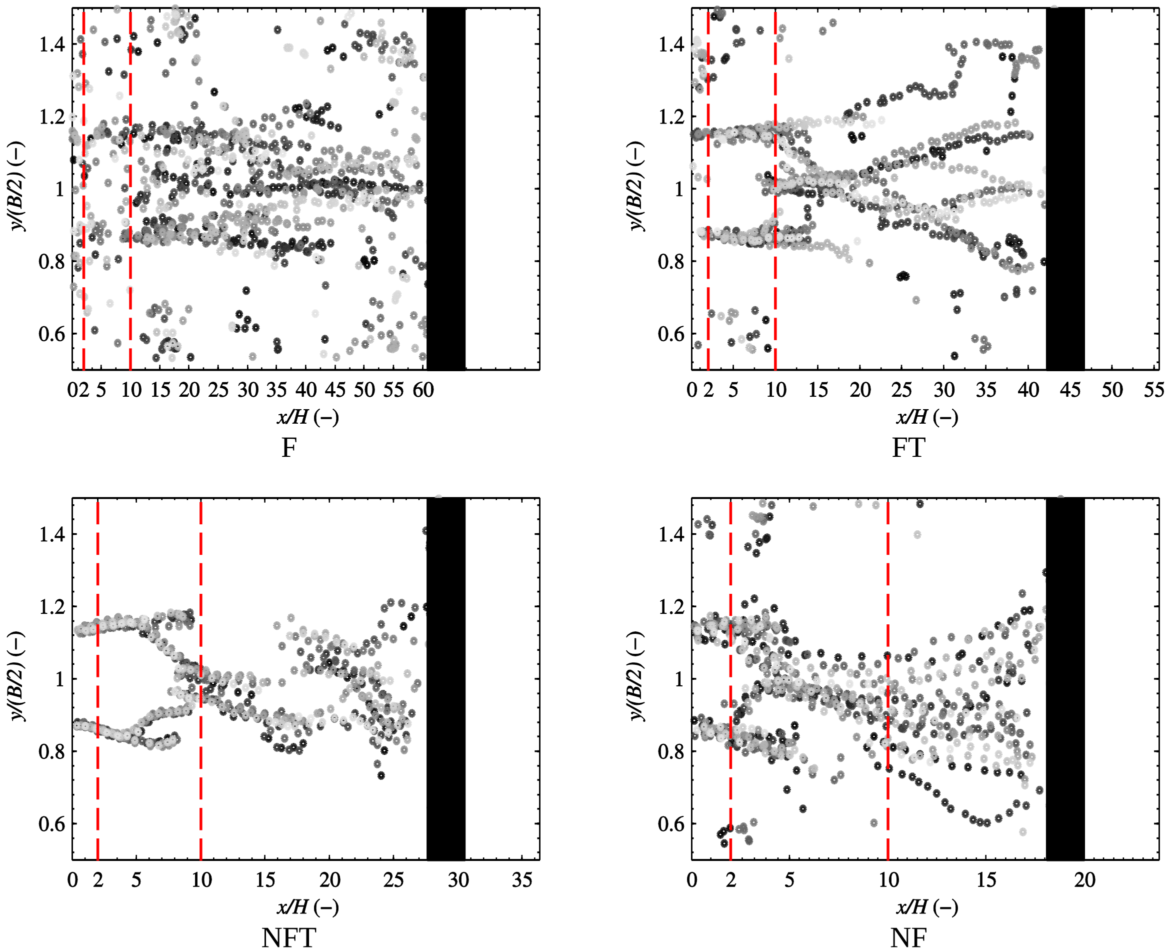

Fig. 10. Depth-normalised positions of the centres of the coherent structures in the 4 flow-cases during 500s. The topology algorithm was applied on the reconstructed velocity fields. The gradient of colour indicates the time evolution, *i.e.* the darkest circles corresponds to the first seconds and the brightest circles corresponds to the last seconds. The vertical dashed lines correspond to x/H = 2 (limit between the near-field and the middle-field of the jet) and x/H = 10 (limit between the middle-field and the far-field of the jet).

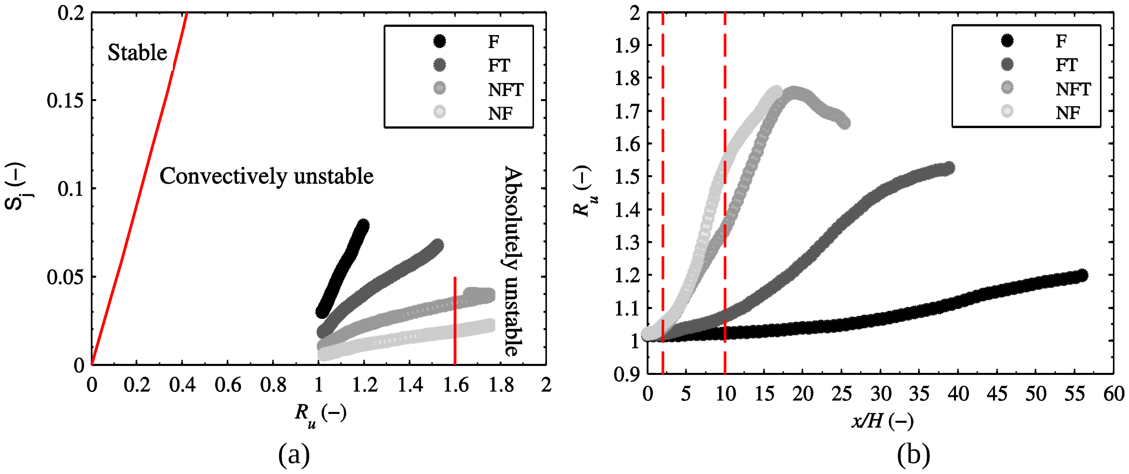

Fig. 11. (a) Stability diagram (S_j, R_u) for the sinuous mode . The red lines correspond to the limit defined in Socolofsky and Jirka (2004). (b) Evolution of the estimation of R_u as a function of the streamwise distance.

Tab. 1. Main characteristics of the measured flows.

Test ID	Q (L/s)	H (cm)	$U_{in} = Q/(Hb)$ (m/s)	F	R	S	Friction regime
F	0.125	1.25	0.13	0.36	4766	0.18	Frictional
FT	0.250	1.80	0.17	0.41	8456	0.10	Frictional close Transition
NFT	0.500	2.75	0.23	0.44	14878	0.06	Non-Frictional close Transition
NF	1.000	4.20	0.30	0.46	24267	0.03	Non-Frictional

Tab. 2. Maximal distance for which the symmetric vortices are observed in spatial modes 1 and 2.

Test ID	S	Friction regime	Maximal distance
F	0.18	Frictional	$40 < x/H < 45$
FT	0.10	Frictional close Transition	$20 < x/H < 25$
NFT	0.06	Non-Frictional close Transition	$15 < x/H < 17$
NF	0.03	Non-Frictional	$5 < x/H < 7$